Quantifying translational and bond-orientational order metrics in hyperuniform and nonhyperuniform many-particle systems

Anirban Mukherjee [1] and Salvatore Torquato [1,2,3,4]

[1]*Department of Physics, Princeton University, Princeton, New Jersey 08544, USA*
[2]*Department of Chemistry, Princeton University, Princeton, New Jersey 08544, USA*
[3]*Princeton Materials Institute, Princeton University, Princeton, New Jersey 08544, USA*
[4]*Program in Applied and Computational Mathematics, Princeton University, Princeton, New Jersey 08544, USA*

(Received 3 September 2026; accepted 2 October 2026; published 19 October 2026)

Quantifying the degree of order and disorder in many-particle systems remains an outstanding problem in physics, materials science, and mathematics. To this end, we consider the translational order metric τ_T, defined as the squared L^2 norm of the total correlation function $h(\mathbf{r})$, and introduce its bond-orientational analog τ_O, defined from the weighted total correlation function $h_{\mathbf{f}}(\mathbf{r})$ using local orientational weights [S. Torquato *et al.*, Phys. Rev. X **16**, 011042 (2026)]. Unlike conventional metrics that quantify either positional order or spatially averaged orientational order, the pair (τ_T, τ_O) places both forms of order on a common two-point statistical footing, with each sensitive to the amplitude and spatial persistence of the corresponding correlation function. The translational order metric τ_T vanishes for a Poisson point process, whereas the geometry-derived weights yield a small, construction-dependent positive reference value of τ_O; each metric diverges in systems possessing its corresponding form of long-range order. We compute both metrics for two nonhyperuniform sphere-packing models in two and three dimensions as functions of packing fraction ϕ: (1) equilibrium hard particles along the stable fluid branches up to near freezing and at selected values of ϕ along the stable crystal branches, and (2) nonequilibrium random sequential addition (RSA) packings from the dilute regime to just below saturation. For the nonhyperuniform systems, bond-orientational order remains subdominant along the equilibrium-fluid and RSA configurations; however, its magnitude relative to the translational metric increases near the upper end of the equilibrium-fluid branches, much more strongly in two than in three dimensions, and the two metrics become comparable along the sampled crystal branches. At common packing fractions, equilibrium fluids and RSA packings trace distinct (τ_T, τ_O) trajectories, revealing preparation-dependent differences in structural order. As a representative hyperuniform family, we study 2D disordered stealthy hyperuniform (SHU) ground states for $0 < \chi < 1/2$, where χ is the stealthiness parameter. Within the disordered SHU phase, bond-orientational order remains subdominant, but its magnitude relative to the translational metric increases toward the disorder-to-order threshold. In all three models, τ_T and τ_O are positively correlated beyond the Poisson-reference regime: τ_O increases monotonically with τ_T across the sampled state points. These metrics may ultimately serve as collective structural coordinates for mapping freezing, melting, glass formation, jamming, self-assembly, and driven nonequilibrium transitions, as well as for enhanced sampling, phase classification, and inverse design.

DOI: 10.1103/llpj-y81h

I. INTRODUCTION

Long-range translational and bond-orientational order are defining properties of perfect crystals and quasicrystals [1–5]. In crystals these forms of order arise from periodic translational symmetry, whereas in quasicrystals they arise from quasiperiodic translational symmetry that permits noncrystallographic rotational symmetries [6]. Between these perfectly ordered systems and the perfectly disordered ideal gas lies a broad range of many-particle systems that lack the full long-range order of perfect crystals and quasicrystals, but whose degrees of order span a continuous spectrum from complete disorder to perfect order [7,8]. In principle, their complete statistical description is contained in the probability density $P_N(\mathbf{r}^N)$, where $\mathbf{r}^N \equiv \{\mathbf{r}_1, \mathbf{r}_2, \ldots, \mathbf{r}_N\}$ specifies the particle coordinates. However, in practice, it is generally inaccessible for large N, and hence one must settle for reduced but meaningful information, such as a scalar order metric $\psi_N(\mathbf{r}^N)$ [7,9,10].

Several scalar translational order metrics have been defined as functionals of the pair correlation function $g_2(\mathbf{r})$ and the total correlation function $h(\mathbf{r})$, related as $h(\mathbf{r}) = g_2(\mathbf{r}) - 1$. The metric T [7,8] measures translational order relative to a perfect face-centered cubic (fcc) lattice at the same number density. The metric T^* [8] integrates $|h(r)|$ over a finite real-space cutoff. The excess two-particle entropy $s^{(2)}$ [8,11] is the leading pair contribution to the excess entropy relative to an ideal gas at the same number density. These metrics have been applied to hard-sphere packings, Lennard-Jones fluids, and liquid water [8,12–14] to characterize the degree of translational order in the disordered phase.

On the other hand, the degree of global bond-orientational order is commonly quantified by one-point functions constructed from locally defined bond-orientational quantities, such as ψ_n in two dimensions [15–20] and Q_l in three dimensions [21–26]. The global forms ψ_6 and Q_6 were subsequently used as scalar order metrics for hard-disk and hard-sphere

 ©2026 American Physical Society

systems, respectively [9,27]. Unlike the translational order metrics described above, these global quantities are functionals of spatial averages of local bond-orientational weights $\mathbf{f}_j$ attached to each particle j and therefore do not retain information about how bond-orientational correlations vary with the separation between particles.

Here we propose to quantify the degrees of global translational and bond-orientational order via metrics that are functionals of their respective two-point correlation functions for statistically homogeneous many-particle configurations whose particle coordinates are fully specified by their centers of mass. The translational order metric τ_T is the squared L^2 norm of the total correlation function:

$$\tau_T = \frac{1}{D^d}\int_{\mathbb{R}^d} h^2(\mathbf{r})\, d\mathbf{r}, \tag{1a}$$

$$= \frac{1}{(2\pi)^d D^d}\int_{\mathbb{R}^d} \widetilde{h}^2(\mathbf{k})\, d\mathbf{k}, \tag{1b}$$

where D is a characteristic length scale and $\widetilde{h}(\mathbf{k})$ is the Fourier transform of the total correlation function $h(\mathbf{r})$. For square-integrable correlation functions, the two representations of this metric are equivalent by Parseval's theorem [28] and enable accurate characterization of short-range translational correlations in direct space [Eq. (1a)] and long-wavelength translational correlations in Fourier space [Eq. (1b)] [29,30]. This metric was introduced in Ref. [28] and subsequently applied to quantify translational order in several disordered systems [31,32]. The translational metric vanishes for a Poisson point process but diverges for perfect crystals and quasicrystals in the thermodynamic limit. For finite periodic or quasiperiodic systems, τ_T grows with system size L, and its rate of growth can be used to distinguish the degree of order among these ordered structures [33,34].

As a bond-orientational analog of τ_T, we introduce the metric τ_O, defined as

$$\tau_O = \frac{1}{D^d |\mathbf{f}|^4_{\text{ref}}}\int_{\mathbb{R}^d} |h_{\mathbf{f}}(\mathbf{r})|^2\, d\mathbf{r}, \tag{2a}$$

$$= \frac{1}{(2\pi)^d D^d |\mathbf{f}|^4_{\text{ref}}}\int_{\mathbb{R}^d} |\widetilde{h}_{\mathbf{f}}(\mathbf{k})|^2\, d\mathbf{k}, \tag{2b}$$

where $h_{\mathbf{f}}(r)$ is the bond-orientationally weighted total correlation function [35], and $|\mathbf{f}|_{\text{ref}}$ is the magnitude of the local orientational weight in a compatible perfect reference crystal. The normalization by $|\mathbf{f}|^4_{\text{ref}}$ makes τ_O invariant under any uniform rescaling of the bond-orientational weights. As with τ_T, the equivalent direct-space [Eq. (2a)] and Fourier-space [Eq. (2b)] representations of τ_O capture both short- and long-wavelength bond-orientational correlations. Unlike τ_T, the bond-orientational metric can possess a nonzero Poisson baseline because the construction of the local bond-orientational weights depends on the identification of geometric neighbors, which can be shared by nearby particles even in an otherwise uncorrelated point pattern. For perfect crystals and quasicrystals, Bragg peaks in the bond-orientational structure factor cause τ_O to diverge in the thermodynamic limit.

The order metrics defined by relations (1) and (2) place translational and bond-orientational order on a common two-point footing (i.e., each metric is constructed from its respective two-point correlation function), which heretofore has not been done. We compute the order metrics for models that span from typical nonhyperuniform systems to hyperuniform ones. As representatives of nonhyperuniform models, which do not anomalously suppress infinite-wavelength density fluctuations [36], we study equilibrium hard-particle configurations [1] and nonequilibrium random sequential addition (RSA) packings [37] in two and three dimensions, using the packing fraction ϕ as the control parameter. The equilibrium configurations span the stable fluid branches up to just short of freezing and are sampled at selected values along the stable crystal branches, whereas the RSA packings extend from the dilute regime to just below saturation. Hyperuniform systems anomalously suppress infinite-wavelength density fluctuations, as expressed by the vanishing of the structure factor in the small-wave-number limit, $S(\mathbf{k}) \to 0$ as $|\mathbf{k}| \to 0$ [36] (see Sec. II C for details). Stealthy hyperuniform systems satisfy the stronger condition $S(\mathbf{k}) = 0$ for $0 < |\mathbf{k}| \leqslant K$ [38], where K is the stealthy cutoff wave number [28]. The dimensionless stealthiness parameter is $\chi = M(K)/[d(N-1)]$, where $M(K)$ is the number of independently constrained wave vectors. As a representative hyperuniform model, we study two-dimensional (2D) SHU ground-state configurations in the disordered regime $0 < \chi < 1/2$, where $\chi = 1/2$ marks the disorder-to-order threshold.

We select these models to determine how global translational and bond-orientational order develop along qualitatively different routes to structural organization. Equilibrium hard particles provide crystallizing nonhyperuniform systems with dimension-dependent [1,39] ordering pathways. RSA packings provide nonequilibrium nonhyperuniform systems that become kinetically arrested without crystallizing [37]. Disordered SHU ground-state configurations allow us to examine how the two global order metrics vary within the disordered SHU phase as χ is increased [28]. We restrict the SHU case to two dimensions as a representative case because the disorder-to-order threshold at $\chi = 1/2$ holds in both two and three dimensions [28]. Antihyperuniform disordered point configurations [40] are not considered here.

In all cases, τ_T and τ_O are positively correlated across the sampled state points, meaning that τ_O increases monotonically with τ_T as the relevant control parameter is varied. Along the equilibrium fluid branches of the sphere packings and within the disordered SHU phase, bond-orientational order remains subdominant to translational order throughout the sampled ranges. As the 2D hard-disk liquid-hexatic coexistence interval is approached from below [39], the sensitivity of τ_O to ϕ increases sharply. A similar, but weaker, increase in the sensitivity of τ_O to χ occurs as the nominal SHU disorder-to-order threshold is approached. Along the sampled equilibrium crystal branches of the sphere packings, the two forms of order become comparable in magnitude. For RSA packings, which undergo no ordering transition, bond-orientational order remains subdominant throughout the full range of packing fractions studied.

In all systems and control-parameter ranges sampled here, τ_T is larger than τ_O and therefore provides a natural reference scale for comparing their relative magnitudes. Accordingly, we use the ratio τ_O/τ_T to distinguish regimes in which bond-orientational order is subdominant, $\tau_O/\tau_T \ll 1$, from those in which the two forms of order are comparable, $\tau_O/\tau_T = O(1)$.

Along the sampled crystal branches, $\tau_O/\tau_T \approx 0.5$–$1$. This ratio quantifies relative magnitude and is distinct from the positive correlation between the metrics, which refers to their monotonic covariation along a control-parameter path. The observed hierarchy $\tau_O < \tau_T$ is specific to the systems sampled here and is not a general constraint. For example, in a hexatic phase, where bond-orientational order is quasi-long-ranged while translational order remains short-ranged [16,35], τ_O may exceed τ_T. More broadly, the pair (τ_T, τ_O) may provide complementary structural objectives for future inverse-design studies seeking prescribed combinations of translational and bond-orientational order [41,42].

The remainder of this paper is organized as follows. In Sec. II we provide background definitions and introduce τ_T and τ_O. Section III describes the model systems and computational methods. In Sec. IV we present and discuss our results. Concluding remarks are given in Sec. V.

II. BACKGROUND AND DEFINITIONS

A. Pair statistics and the structure factor

For an N-particle system in d-dimensional Euclidean space $\mathbb{R}^d$, with configuration $\mathbf{r}^N \equiv (\mathbf{r}_1, \ldots, \mathbf{r}_N)$, the reduced n-particle density functions are obtained from the configurational probability density $P_N(\mathbf{r}^N)$ by integrating over all but n particle coordinates [1,2]:

$$\rho_n(\mathbf{r}^n) = \frac{N!}{(N-n)!} \int \cdots \int P_N(\mathbf{r}^N)\, d\mathbf{r}_{n+1} \cdots d\mathbf{r}_N. \tag{3}$$

The corresponding n-particle correlation functions are

$$g_n(\mathbf{r}^n) = \frac{\rho_n(\mathbf{r}^n)}{\rho^n}, \tag{4}$$

where ρ is the number density. For statistically homogeneous systems, the pair correlation function is

$$g_2(\mathbf{r}_{12}) = \frac{\rho_2(\mathbf{r}_{12})}{\rho^2}, \tag{5}$$

where $\mathbf{r}_{12} = \mathbf{r}_2 - \mathbf{r}_1$. The total correlation function,

$$h(\mathbf{r}) = g_2(\mathbf{r}) - 1, \tag{6}$$

measures the deviation of the pair statistics from those of an uncorrelated system. For statistically isotropic systems, g_2 and h depend only on $r = |\mathbf{r}|$, and $g_2(r)$ is the radial distribution function.

We define the Fourier transform of a function $f(\mathbf{r})$ as [40]

$$\tilde{f}(\mathbf{k}) = \int_{\mathbb{R}^d} f(\mathbf{r})\, e^{-i\mathbf{k}\cdot\mathbf{r}}\, d\mathbf{r}, \tag{7}$$

with inverse

$$f(\mathbf{r}) = \frac{1}{(2\pi)^d} \int_{\mathbb{R}^d} \tilde{f}(\mathbf{k})\, e^{i\mathbf{k}\cdot\mathbf{r}}\, d\mathbf{k}. \tag{8}$$

The structure factor is related to the Fourier transform of the total correlation function by [1,2]

$$S(\mathbf{k}) = 1 + \rho\, \tilde{h}(\mathbf{k}). \tag{9}$$

It is proportional to the scattering intensity and is directly accessible in scattering experiments [1]. For statistically isotropic systems, $S(\mathbf{k})$ depends only on $k = |\mathbf{k}|$. An ideal gas has $h(r) = 0$ and $S(k) = 1$, whereas a perfect crystal exhibits Bragg peaks at reciprocal lattice vectors.

B. Translational order metric

In statistically isotropic systems, $h(\mathbf{r})$ and $\tilde{h}(\mathbf{k})$ become functions only of the magnitudes $r = |\mathbf{r}|$ and $k = |\mathbf{k}|$, respectively, and we can write τ_T in Eq. (1) as

$$\tau_T = \frac{s_1(1)}{D^d} \int_0^\infty h^2(r)\, r^{d-1}\, dr, \tag{10a}$$

$$= \frac{s_1(1)}{(2\pi)^d D^d} \int_0^\infty \tilde{h}^2(k)\, k^{d-1}\, dk, \tag{10b}$$

where $s_1(1) = 2\pi^{d/2}/\Gamma(d/2)$ is the surface area of the unit sphere in d dimensions. For an ideal gas, or spatially uncorrelated Poisson point process, $h(r) = 0$, equivalently $\tilde{h}(k) = 0$, and hence $\tau_T = 0$. Thus, deviations of τ_T from zero measure the degree of translational order relative to the fully uncorrelated case.

For comparison with the numerical results, we use three analytical references. For equilibrium and RSA hard-particle systems, the dilute-limit pair correlation function is $g_2(r) = \Theta(r - 2R) + O(\phi)$, where R is the particle radius [2]. Substitution of $h(r) = g_2(r) - 1$ into Eq. (10a) gives the dilute-limit reference $\tau_T^{\text{dilute}} = 2^d\phi$. For three-dimensional (3D) equilibrium hard spheres, τ_T^{PY} is obtained analogously using the Percus-Yevick approximation [2]. For 2D disordered SHU ground states, using the choice $D = \rho^{-1/d}$ adopted in this work, the small-χ prediction is $\tau_T = 4\chi + O(\chi^2)$ as $\chi \to 0$ [28].

For the disordered systems considered here, $h \in L^2$, and the integrals in Eqs. (10a) and (10b) are well defined in the thermodynamic limit. However, in the crystal phases, quasi-long-range translational order in two dimensions and long-range translational order in three dimensions imply that $h \notin L^2$ in the thermodynamic limit [15,16,34,39]. We therefore evaluate the cutoff-dependent quantity $\tau_T(K_c; L)$,

$$\tau_T(K_c; L) \equiv \frac{s_1(1)}{(2\pi)^d D^d} \int_0^{K_c} \tilde{h}^2(k)\, k^{d-1}\, dk, \tag{11}$$

where K_c is an imposed radial wave number cutoff and

$$\tilde{h}(k) = \frac{1}{\Omega} \int_\Omega \tilde{h}(\mathbf{k})\, d\Omega \tag{12}$$

denotes the angular average at fixed k, with $\Omega = s_1(1)$. At fixed system size L, $\lim_{K_c \to \infty} \tau_T(K_c; L) = \tau_T(L)$, whereas the cutoff-converged value $\tau_T(L)$ remains system-size dependent and diverges as $L \to \infty$ [33,34]. Here $\tau_T(L)$ denotes the finite-system equilibrium quantity at fixed L, whereas its numerical estimate is obtained from the shell- and, when available, ensemble-averaged structure factor.

C. Hyperuniformity and the number variance

A statistically homogeneous and isotropic many-particle system is said to be *hyperuniform* if its local number variance $\sigma^2(R)$ within a spherical observation window of radius R grows more slowly than the window volume in the large-R

limit [36]. Equivalently, the structure factor satisfies

$$\lim_{k\to 0} S(k) = 0. \tag{13}$$

Thus, hyperuniform systems suppress infinite-wavelength density fluctuations. If the structure factor vanishes near the origin as

$$S(k) \sim k^{\alpha} \quad (k \to 0,\ \alpha > 0), \tag{14}$$

then the large-R scaling of the local number variance is

$$\sigma^2(R) \sim \begin{cases} R^{d-1}, & \alpha > 1 \quad \text{(class I)}, \\ R^{d-1}\ln R, & \alpha = 1 \quad \text{(class II)}, \\ R^{d-\alpha}, & 0 < \alpha < 1 \quad \text{(class III)}. \end{cases} \tag{15}$$

Classes I and III represent the strongest and weakest forms of hyperuniformity, respectively. Perfect crystals and disordered SHU ground states provide ordered and disordered examples of class I hyperuniformity. By contrast, typical nonhyperuniform systems have $\sigma^2(R) \sim R^d$, corresponding to a positive finite limit of $S(k)$ as $k \to 0$. Antihyperuniform systems, for which $\sigma^2(R)$ grows faster than R^d, are not considered here.

D. Weighted bond-orientational correlations

We use the weighted-particle formalism of Torquato *et al.* [35] to describe bond-orientational correlations. Each particle j at position $\mathbf{r}_j$ carries a weight $\mathbf{f}_j$ that encodes its local bond-orientational environment. A bond is the center-to-center connection between a particle and one of its prescribed nearest neighbors, whose construction is specified in Sec. III D.

In two dimensions we use the sixfold bond-orientational order parameter as a complex scalar weight:

$$f_j \equiv \psi_6(j) = \frac{1}{N_j}\sum_{k=1}^{N_j} \exp(i6\theta_{jk}), \tag{16}$$

where N_j is the number of prescribed nearest neighbors of particle j, and θ_{jk} is the angle, measured relative to a fixed reference axis, of the bond joining particle j to its kth neighbor. In three dimensions we use the complex vector weight

$$\mathbf{f}_j = \{Q_{6m}(j)\}_{m=-6}^{6}, \tag{17}$$

where

$$Q_{lm}(j) \equiv \sqrt{\frac{4\pi}{2l+1}}\,\frac{1}{N_j}\sum_{k=1}^{N_j} Y_{lm}(\theta_{jk},\varphi_{jk}), \tag{18}$$

and $Y_{lm}(\theta,\varphi)$ is the spherical harmonic of degree l and order m. We choose $l = 6$ because the corresponding order parameter Q_6 is known to detect fcc bond-orientational ordering [7]. The normalizations in Eqs. (16) and (18) ensure that the magnitude of the local orientational weight does not exceed unity in either dimension.

For statistically homogeneous weighted particle systems, let $p(\mathbf{f})$ denote the singlet probability density of the weights and $\rho_2(\mathbf{r};\mathbf{f}_1,\mathbf{f}_2)$ the two-particle probability density at separation $\mathbf{r}$. Following Ref. [35], the generalized pair correlation function is

$$g_{2;\mathbf{f}}(\mathbf{r};\mathbf{f}_1,\mathbf{f}_2) \equiv \frac{\rho_2(\mathbf{r};\mathbf{f}_1,\mathbf{f}_2)}{\rho^2}. \tag{19}$$

In the absence of long-range order, $g_{2;\mathbf{f}}(\mathbf{r};\mathbf{f}_1,\mathbf{f}_2) \to p(\mathbf{f}_1)p(\mathbf{f}_2)$ as $|\mathbf{r}| \to \infty$. The weight-averaged pair correlation function is

$$g_{2;\mathbf{f}}(\mathbf{r}) \equiv \iint (\mathbf{f}_1^{\dagger} \bullet \mathbf{f}_2)\, g_{2;\mathbf{f}}(\mathbf{r};\mathbf{f}_1,\mathbf{f}_2)\, d\mathbf{f}_1\, d\mathbf{f}_2, \tag{20}$$

where $\bullet$ denotes an inner product. For the weights used here,

$$\mathbf{f}_1^{\dagger} \bullet \mathbf{f}_2 = \begin{cases} \psi_6^*(1)\psi_6(2), & d = 2, \\ \sum_{m=-6}^{6} Q_{6m}^*(1)Q_{6m}(2), & d = 3. \end{cases} \tag{21}$$

This inner product measures the similarity of the local bond-orientational environments and is invariant under a global rotation. The corresponding weighted total correlation function is

$$h_{\mathbf{f}}(\mathbf{r}) \equiv g_{2;\mathbf{f}}(\mathbf{r}) - |\langle\mathbf{f}\rangle|^2, \tag{22}$$

where $\langle\mathbf{f}\rangle = \int \mathbf{f}\, p(\mathbf{f})\, d\mathbf{f}$. From Eq. (20), particle-exchange symmetry implies that $h_{\mathbf{f}}(\mathbf{r})$ satisfies

$$h_{\mathbf{f}}(-\mathbf{r}) = h_{\mathbf{f}}^*(\mathbf{r}). \tag{23}$$

For statistically isotropic systems, $h_{\mathbf{f}}(-\mathbf{r}) = h_{\mathbf{f}}(\mathbf{r}) = h_{\mathbf{f}}(r)$, and Eq. (23) therefore implies that $h_{\mathbf{f}}(r)$ is real.

Although $h_{\mathbf{f}}(\mathbf{r})$ is a two-point correlation function of the weighted field, the geometry-derived weights depend on local particle neighborhoods and therefore encode higher-order positional information from the underlying unweighted configuration.

E. Bond-orientational order metric

The bond-orientational order metric τ_O is defined in Eqs. (2a) and (2b). The normalization by $|\mathbf{f}|_{\text{ref}}^4$ makes τ_O invariant under a uniform rescaling of the orientational weights, where $|\mathbf{f}|_{\text{ref}}$ is the magnitude of the local bond-orientational weight in the corresponding perfect reference crystal. In statistically isotropic systems, $h_{\mathbf{f}}(\mathbf{r})$ and $\tilde{h}_{\mathbf{f}}(\mathbf{k})$ become functions only of the magnitudes $r = |\mathbf{r}|$ and $k = |\mathbf{k}|$, respectively, and are real. We can therefore write τ_O in Eq. (2) as

$$\tau_O = \frac{s_1(1)}{D^d|\mathbf{f}|_{\text{ref}}^4}\int_0^{\infty} [h_{\mathbf{f}}(r)]^2 r^{d-1}\, dr, \tag{24a}$$

$$= \frac{s_1(1)}{(2\pi)^d D^d|\mathbf{f}|_{\text{ref}}^4}\int_0^{\infty} [\tilde{h}_{\mathbf{f}}(k)]^2 k^{d-1}\, dk. \tag{24b}$$

The square-integrability and convergence conditions for the disordered systems are the same as for τ_T in Sec. II B, with h replaced by $h_{\mathbf{f}}$. For the crystal phases considered here, $h_{\mathbf{f}}$ inherits the non-square-integrable crystalline correlations because the bond-orientational weights remain coherently ordered over long distances in both two and three dimensions [16,21]. We therefore report the radial cutoff-dependent quantity

$$\tau_O(K_c;L) \equiv \frac{s_1(1)}{(2\pi)^d D^d|\mathbf{f}|_{\text{ref}}^4}\int_0^{K_c} |\tilde{h}_{\mathbf{f}}(k)|^2 k^{d-1}\, dk, \tag{25}$$

where

$$\tilde{h}_{\mathbf{f}}(k) = \frac{1}{\Omega}\int_{\Omega} \tilde{h}_{\mathbf{f}}(\mathbf{k})\, d\Omega \tag{26}$$

is the angularly averaged radial function, with $\Omega = s_1(1)$. At fixed system size L, $\lim_{K_c\to\infty} \tau_O(K_c;L) = \tau_O(L)$, whereas the

cutoff-converged value $\tau_O(L)$ remains system-size dependent and diverges as $L \to \infty$. Here $\tau_O(L)$ denotes the finite-system equilibrium quantity at fixed L, whereas its numerical estimate is obtained from the shell- and, when available, ensemble-averaged bond-orientational structure factor. For the corresponding perfect reference crystal, $\mathbf{f}_j = \mathbf{f}_{\rm ref}$ at every particle site. It then follows from Eqs. (20) and (22) that the angularly averaged functions $h_{\mathbf{f}}(r)$ and $h(r)$ are related by $h_{\mathbf{f}}(r) = |\mathbf{f}|^2_{\rm ref} h(r)$ and, consequently, $\tilde{h}_{\mathbf{f}}(k) = |\mathbf{f}|^2_{\rm ref}\tilde{h}(k)$. Therefore, comparing Eqs. (11) and (25), we obtain

$$\tau_O(K_c; L) = \tau_T(K_c; L) \tag{27}$$

for any common radial wave-number cutoff K_c and system size L.

III. MODEL SYSTEMS AND COMPUTATIONAL METHODS

A. Equilibrium hard-particle systems

We study 2D hard disks and 3D hard spheres along their stable fluid branches up to just short of freezing and at selected packing fractions along their stable crystal branches. The control parameter is the packing fraction

$$\phi = \rho v_1(R), \tag{28}$$

where ρ is the number density, R is the particle radius, and $v_1(R) = \pi^{d/2}R^d/\Gamma(1 + d/2)$ is the volume of a d-dimensional sphere of radius R. The target-state configurations are equilibrated in the canonical ensemble under periodic boundary conditions using the preparation protocols described below. Before evaluating τ_T and τ_O, the particle coordinates, particle radii, and simulation box are uniformly rescaled to unit number density, $\rho = 1$.

We consider both $d = 2$ and $d = 3$ because their crystallization pathways differ qualitatively. With increasing packing fraction, 2D hard disks undergo a first-order liquid-hexatic transition with a narrow coexistence interval, $0.700 \lesssim \phi \lesssim 0.716$, followed by a continuous hexatic-solid transition near $\phi \approx 0.720$ [39]. Within the hexatic phase, bond-orientational correlations are quasi-long-ranged, whereas translational correlations remain short-ranged. By contrast, 3D hard spheres undergo a first-order fluid-crystal transition with coexistence between the fluid freezing value $\phi_F \approx 0.494$ and the crystal melting value $\phi_M \approx 0.545$, without an analogous intermediate phase [2]. This dimensional contrast allows us to compare how translational and bond-orientational order develop along the fluid and crystal branches, away from the transition regions, in systems with qualitatively different crystallization pathways.

1. *Fluid branches of equilibrium hard disks and hard spheres*

For 2D hard disks, we use systems with $N = 10\,000$ particles over $0.01 \leqslant \phi \leqslant 0.68$. For 3D hard spheres, we use systems with $N = 100\,000$ particles over $0.01 \leqslant \phi \leqslant 0.49$. These ranges extend from the dilute regime to just below the respective freezing transitions.

Direct RSA configurations at the target packing fraction were used as initial conditions whenever they could be generated efficiently. For $0.01 \leqslant \phi < 0.50$ in two dimensions and $0.01 \leqslant \phi \leqslant 0.19$ in three, RSA configurations were generated directly at the target packing fraction and subsequently equilibrated. For $0.50 \leqslant \phi \leqslant 0.68$ in two dimensions, an RSA configuration at $\phi = 0.40$ was used as the initial state, whereas for $0.20 \leqslant \phi \leqslant 0.49$ in three, an RSA configuration at $\phi = 0.10$ was used. In both cases, the particles were grown isotropically to the target packing fraction [43] before equilibration. At each state point, 10 000 and 1000 equilibrated configurations were sampled for the 2D and 3D systems, respectively.

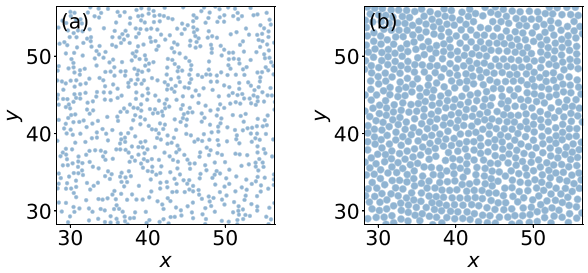


FIG. 1. Representative fluid-branch configurations of 2D equilibrium hard disks at (a) $\phi = 0.20$ and (b) $\phi = 0.68$, each displaying the same area and containing approximately 800 disk centers. The higher-packing-fraction configuration exhibits stronger short-range positional correlations.

Representative 2D fluid configurations at low and near-freezing packing fractions are shown in Fig. 1.

2. *Crystal branches of equilibrium hard disks and hard spheres*

For 2D hard disks, we use systems with $N = 160\,000$ particles in a rhombic periodic box compatible with a triangular crystal. We study the packing fractions $\phi = 0.75$, 0.77, 0.79, and 0.81 along the stable solid branch. At each target packing fraction, an RSA configuration at $\phi = 0.30$ was used as the initial state. The system was isotropically compressed to the target packing fraction and subsequently equilibrated using a Monte Carlo algorithm [44]. Only the final equilibrated configuration was used for the structural analysis, after verifying that it contained no polycrystalline grains and exhibited true long-range bond-orientational correlations. Representative 2D crystal configurations are shown in Fig. 2.

For 3D hard spheres, we use systems with $N = 108\,000$ particles in a cubic periodic box compatible with an fcc crystal. We study the packing fractions $\phi = 0.56$, 0.60, 0.65, and

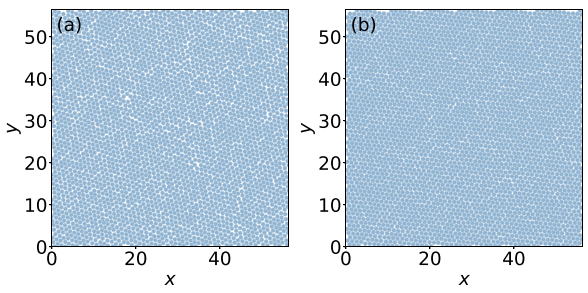


FIG. 2. Representative crystal-branch configurations of 2D equilibrium hard disks at (a) $\phi = 0.75$ and (b) $\phi = 0.81$, each displaying the same area and containing approximately 3200 disk centers. The density of lattice defects is lower at the higher packing fraction.

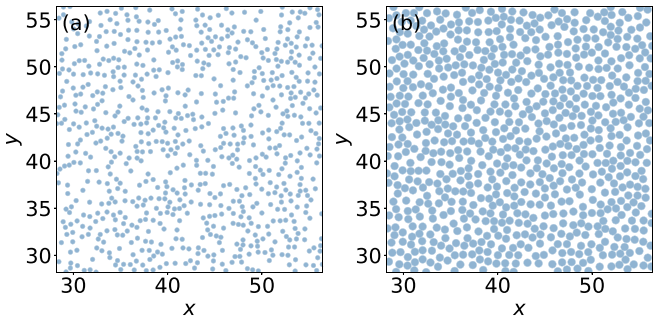


FIG. 3. Representative 2D RSA hard-disk configurations at (a) $\phi = 0.20$ and (b) $\phi = 0.54$, each displaying the same area and containing approximately 800 disk centers. The higher-packing-fraction configuration exhibits stronger short-range exclusion-induced correlations.

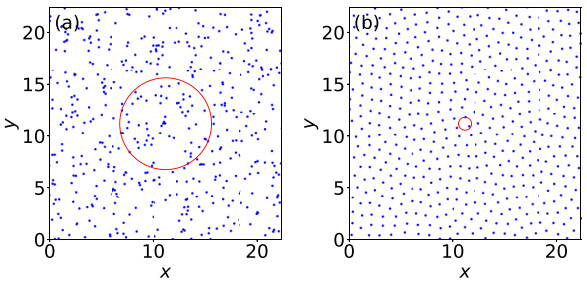


FIG. 4. Representative 2D disordered SHU ground-state configurations at (a) $\chi = 0.01$ and (b) $\chi = 0.495$. Each panel displays the same area and contains approximately 500 points. The circle indicates the stealthy wavelength $\lambda = 2\pi/K$. The greater structural regularity at the larger value of χ is visible.

0.70 along the stable crystal branch. At each packing fraction, ten independent trajectories were initialized from a perfect fcc configuration constructed directly at the target packing fraction and equilibrated using a Monte Carlo algorithm [44]. The final equilibrated configuration from each trajectory was used for the structural analysis.

B. Random sequential addition packings

We next consider RSA packings, which provide nonequilibrium systems that approach saturation without crystallizing. Starting from an empty periodic simulation box, particles are inserted randomly and sequentially, with any placement that overlaps a previously accepted particle rejected. The process continues until the target number of particles is accepted. At saturation, no additional particle can be inserted without overlap. Saturated RSA packings are statistically isotropic and nonhyperuniform, with $\lim_{k\to 0} S(k) > 0$ in finite spatial dimensions [37].

For 2D RSA packings, we use systems with $N = 10\,000$ particles and study packing fractions in the range $0.01 \leqslant \phi \leqslant 0.54$, extending from the dilute regime to just below the saturation value $\phi_s \approx 0.547$. For 3D RSA packings, we use systems with $N = 100\,000$ particles and study $0.01 \leqslant \phi \leqslant 0.37$, extending to just below the saturation value $\phi_s \approx 0.384$ [37]. At each packing fraction, the particle radius was chosen according to the target value of ϕ at unit number density, $\rho = 1$, and the particles were deposited sequentially in a periodic square box in two dimensions or a periodic cubic box in three. We generated 10 000 independent configurations at each state point in two dimensions and 100 independent configurations at each state point in three. Representative 2D RSA configurations at intermediate and near-saturated packing fractions are shown in Fig. 3.

C. Stealthy hyperuniform ground-state configurations

We consider 2D stealthy hyperuniform (SHU) ground-state configurations generated using the collective-coordinate ground-state optimization procedure described in Refs. [28,38,45]. These configurations satisfy

$$S(k) = 0, \quad 0 < k \leqslant K, \tag{29}$$

so that density fluctuations are completely suppressed over the prescribed range of wave numbers. The control parameter is the stealthiness parameter $\chi = M(K)/[d(N-1)]$ [38], where $M(K)$ is the number of independently constrained wave vectors. A larger χ corresponds to a larger value of K and hence greater stealthiness. Correspondingly, in real space, the dimensionless surface-area coefficient governing the asymptotic number variance decreases as χ increases, indicating stronger suppression of large-scale density fluctuations [28].

In the thermodynamic limit, the entropically favored SHU ground states undergo a disorder-to-order transition at $\chi = 1/2$ in both $d = 2$ and $d = 3$ [28]. We study only the isotropic disordered regime in two dimensions as a representative case, using $N = 5000$ particles at unit number density over $0.001 \leqslant \chi \leqslant 0.495$. For each χ, the stealthy cutoff is

$$K = 4\sqrt{\pi\chi}, \tag{30}$$

and 4000 independent configurations are generated from random initial conditions. The collective-coordinate objective is minimized using L-BFGS with an energy tolerance of 10^{-16}. Representative configurations at $\chi = 0.01$ and $\chi = 0.495$ are shown in Fig. 4.

D. Computation of bond-orientational weights and order metrics

The local bond-orientational weights are computed from Eqs. (16)–(18). Nearest neighbors are defined using the periodic Delaunay tessellation for all disordered systems and for the 2D crystal branch. For the 3D fcc crystal branch, we instead use exactly 12 periodic nearest neighbors, corresponding to the physical first coordination shell, because degeneracies in the fcc Delaunay tessellation introduce additional neighbors. The triangular lattice in two dimensions and the fcc lattice in three are the corresponding thermodynamically stable crystalline structures. In Eqs. (2a) and (2b), $|\mathbf{f}|_{\rm ref}$ denotes the magnitude of the local orientational weight in the compatible perfect reference crystal. For the triangular crystal, $\psi_6 = 1$ and hence $|\mathbf{f}|_{\rm ref} = 1$, whereas for the fcc crystal, using the same 12-nearest-neighbor convention,

$$|\mathbf{f}|_{\rm ref} = \left[\sum_{m=-6}^{6} \left|Q_{6m}^{\rm fcc}\right|^2\right]^{1/2} \approx 0.575. \tag{31}$$

Throughout this work, all configurations are expressed at unit number density, $\rho = 1$, before evaluating τ_T and τ_O. The characteristic length, defined as the mean interparticle spacing, is therefore

$$D = \rho^{-1/d} = 1. \tag{32}$$

The equilibrium fluid branches, RSA packings, and disordered SHU ground states are statistically isotropic, whereas the crystal branches are isotropized by angular averaging over reciprocal-space shells. For the equilibrium fluid branches and RSA packings, we compute $h(r)$ and $h_{\mathbf{f}}(r)$ directly and evaluate the isotropic direct-space forms in Eqs. (10a) and (24a). At every state point, the cumulative integrals reach plateaus well below the maximum independent separation allowed by the periodic boundaries, and we report these plateau values.

For the disordered SHU ground-state configurations and crystal branches, we evaluate the metrics in reciprocal space. For a periodic simulation cell, the allowed wave vectors are

$$\mathbf{k} = \sum_{i=1}^{d} n_i \mathbf{b}_i, \tag{33}$$

where $\mathbf{b}_i$ are the reciprocal primitive vectors and n_i are integers. The reciprocal-space integral is replaced by

$$\frac{1}{(2\pi)^d} \int d\mathbf{k} \longrightarrow \frac{1}{V} \sum_{\mathbf{k}}, \tag{34}$$

where V is the volume of the fundamental cell. Using Eq. (9), the isotropized finite-cell translational metric is

$$\tau_T(K_c) = \frac{1}{\rho^2 V D^d} \sum_{0<k_s\leqslant K_c} m(k_s)[\overline{S}(k_s) - 1]^2. \tag{35}$$

Here k_s is the wave-number magnitude associated with shell s, $m(k_s)$ is the number of reciprocal vectors in that shell, $\overline{S}(k_s)$ is the shell- and ensemble-averaged structure factor, and K_c is the radial wave-number cutoff. Equation (35) is the finite-cell discrete approximation to Eq. (11). For the disordered SHU configurations, provided L is sufficiently large that the omitted finite-size contribution is negligible and K_c is sufficiently large, Eq. (35) converges to the thermodynamic-limit form in Eq. (10b).

The weighted collective coordinate and bond-orientational structure factor are

$$\mathbf{F}_{\mathbf{f}}(\mathbf{k}) = \sum_{j=1}^{N} \mathbf{f}_j \exp(-i\mathbf{k}\cdot\mathbf{r}_j),$$

$$S_O(\mathbf{k}) = \frac{1}{N}\langle \mathbf{F}_{\mathbf{f}}^{\dagger}(\mathbf{k}) \bullet \mathbf{F}_{\mathbf{f}}(\mathbf{k})\rangle. \tag{36}$$

For $\mathbf{k} \neq \mathbf{0}$,

$$S_O(\mathbf{k}) - \langle|\mathbf{f}|^2\rangle = \rho\widetilde{h}_{\mathbf{f}}(\mathbf{k}), \tag{37}$$

and hence the isotropized finite-cell bond-orientational metric is

$$\tau_O(K_c) = \frac{1}{\rho^2 V D^d |\mathbf{f}|^4_{\mathrm{ref}}} \sum_{0<k_s\leqslant K_c} m(k_s)|\overline{S}_O(k_s) - \langle|\mathbf{f}|^2\rangle|^2. \tag{38}$$

Here $\overline{S}_O(k_s)$ is the shell- and ensemble-averaged bond-orientational structure factor. The subtraction of $\langle|\mathbf{f}|^2\rangle$ removes the self-contribution, in direct analogy with the subtraction of unity from $S(\mathbf{k})$. Equation (38) is the finite-cell discrete approximation to Eq. (25) and, for the disordered SHU ground-state configurations under the same conditions stated above, converges to the thermodynamic-limit form in Eq. (24b), with τ_O becoming insensitive to further increases in K_c. For the crystal branches, the dependence of $\tau_T(K_c)$ and $\tau_O(K_c)$ on the fixed system size L is implicit. At fixed L, $\lim_{K_c\to\infty} \tau_T(K_c) = \tau_T(L)$ and $\lim_{K_c\to\infty} \tau_O(K_c) = \tau_O(L)$; these cutoff-converged values remain system-size dependent and diverge as $L \to \infty$.

For ensemble-averaged data, the statistical uncertainties in τ_T and τ_O are estimated separately using leave-one-configuration-out jackknife standard errors [46]. In all cases, their noise-to-signal ratios are much smaller than unity, and the growth trends are clear.

IV. RESULTS

A. Interpretation of the order metrics

For each model we examine how the translational and bond-orientational order metrics, τ_T and τ_O, vary along a one-parameter structural pathway: packing fraction ϕ for the equilibrium and RSA sphere packings, and stealthiness parameter χ for the SHU ground states. Throughout the results below, the local orientational weight entering τ_O is $f_j = \psi_6(j)$ in two dimensions [Eq. (16)] and $\mathbf{f}_j = \{Q_{6m}(j)\}_{m=-6}^{6}$ in three [Eq. (17)], with the components $Q_{6m}(j)$ defined in Eq. (18). We characterize each pathway using three complementary quantities: the parametric trajectory in the (τ_T, τ_O) plane, the relative magnitude τ_O/τ_T, and, where useful, the sensitivities E_T and E_O [see Eqs. (39) and (40)]. Here a "positive correlation" means that τ_O increases monotonically with τ_T along the sampled pathway; it does not denote a Pearson, Spearman, or other statistical correlation coefficient. We call bond-orientational order subdominant when $\tau_O/\tau_T \ll 1$ and the two forms of order comparable when this ratio is of order unity. Because τ_O has a small positive Poisson reference while τ_T vanishes in the Poisson limit, we interpret τ_O/τ_T only beyond the Poisson-reference regime (see Appendix B).

We define the sensitivity of each of the two order metrics with respect to the control parameter as

$$E_\alpha \equiv \frac{d\ln\tau_\alpha}{d\ln\lambda} = \frac{\lambda}{\tau_\alpha}\frac{d\tau_\alpha}{d\lambda}, \quad \alpha = T, O, \tag{39}$$

where $\lambda = \phi$ for the equilibrium and RSA sphere packings and $\lambda = \chi$ for the SHU ground states. Thus, a 1% change in λ produces approximately an E_α% change in τ_α. For discretely sampled data, we use the centered finite-difference estimate

$$E_{\alpha,i} \approx \frac{(\tau_{\alpha,i+1} - \tau_{\alpha,i-1})/\tau_{\alpha,i}}{(\lambda_{i+1} - \lambda_{i-1})/\lambda_i}. \tag{40}$$

Representative finite-size diagnostics for the sampled fluid and disordered phases are presented in Appendix A using the control-parameter values closest to their respective ordering thresholds or saturation limits. The 2D and 3D hard-particle correlation functions decay on length scales much smaller than the size of the simulation boxes. For the 2D and 3D equilibrium crystal branches, the small-k behavior of $S(k)$ is consistent with the free-volume-theory prediction [10,47]. In

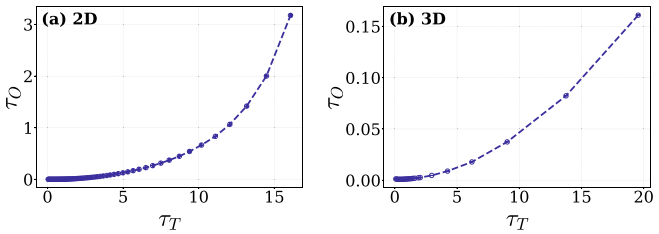


FIG. 5. Parametric relation between τ_O and τ_T along the stable fluid branches of (a) 2D equilibrium hard disks and (b) 3D equilibrium hard spheres. In both dimensions, τ_O increases monotonically with τ_T along the sampled branches.

the SHU ensemble, sufficiently many allowed wave vectors lie within the stealthy region $0 < k \leqslant K$, where $S(k) = 0$, while $S_O(k)$ remains finite down to the smallest nonzero wave number, $k_{\min} = 2\pi/L$, where L is the simulation box side length, and exhibits no apparent long-wavelength divergence. These observations indicate that the system sizes used are sufficient for the reported fluid and disordered-state metrics.

B. Equilibrium sphere packings

Across all sampled equilibrium fluid and crystal branches, τ_O increases monotonically with τ_T; the fluid-branch trajectories are shown in Fig. 5. The magnitude and rate of this increase, however, depend strongly on dimensionality and phase.

1. Stable fluid branch of 2D hard disks

Along the 2D fluid branch, τ_T agrees with its dilute-limit prediction at low ϕ and departs from it as hard-core correlations become appreciable [Fig. 6(a)]. Bond-orientational order remains subdominant throughout the sampled branch, but its magnitude relative to τ_T grows substantially approaching the freezing point: τ_O/τ_T increases from approximately 3.4×10^{-3} at $\phi = 0.20$ to 0.198 at $\phi = 0.68$ [Fig. 6(b)].

This increase results from the sharply increasing sensitivity of τ_O close to the freezing point. Specifically, E_O/E_T increases overall from approximately 1.72 at $\phi = 0.20$ to 4.38 at $\phi = 0.67$ [Fig. 7]. Thus, near the upper end of the sampled stable-fluid branch, orientational correlations strengthen fractionally more rapidly than translational correlations. This enhanced response is consistent with growing orientational organization below the liquid-hexatic coexistence interval,

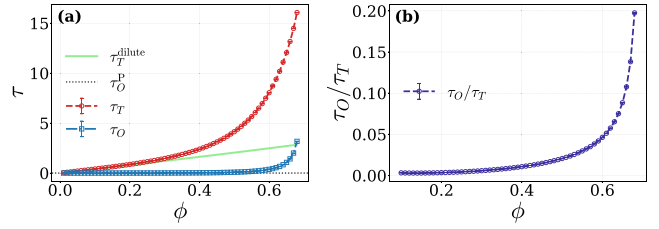


FIG. 6. Along the stable fluid branch of 2D equilibrium hard disks, (a) τ_T and τ_O as functions of ϕ, together with the dilute-limit prediction $\tau_T^{\text{dilute}} = 4\phi$ for τ_T, and (b) the ratio τ_O/τ_T. Although τ_O remains subdominant, its magnitude relative to τ_T increases substantially toward the upper end of the branch.

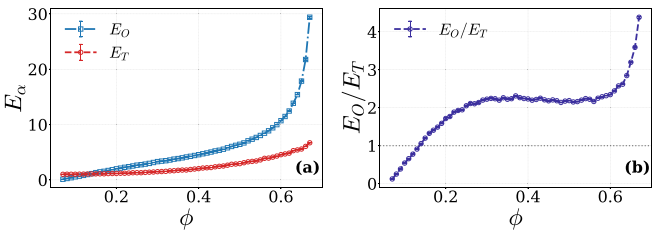


FIG. 7. Sensitivities E_T and E_O and their ratio E_O/E_T along the stable fluid branch of 2D equilibrium hard disks. The larger fractional growth of τ_O, which becomes more pronounced near the upper end of the fluid branch, explains the increase in τ_O/τ_T.

$0.700 \leqslant \phi \leqslant 0.716$ [39], although the present data do not extend into that interval.

2. Stable fluid branch of 3D hard spheres

For the 3D fluid, τ_T approaches the dilute-limit result at low ϕ, while the Percus-Yevick prediction [2] provides an accurate reference over a broader range [Fig. 8(a)]. The ratio τ_O/τ_T increases from approximately 1.3×10^{-3} at $\phi = 0.20$ to 8.2×10^{-3} at $\phi = 0.49$, remaining below 1% throughout the sampled range beyond the Poisson-reference regime [Fig. 8(b)]. The enhancement observed in the 2D fluid is therefore absent in three dimensions: translational and bond-orientational correlations remain short-ranged, and τ_O remains very small relative to τ_T. Because the ratio exhibits no comparably pronounced increase, we do not apply the fractional-response analysis to this branch.

3. Crystal branches

In the crystal branches, we use the radial cutoff-dependent definitions in Eqs. (11) and (25), and both metrics depend on the common radial wave-number cutoff K_c. To simplify notation, throughout this subsection $\tau_T(K_c)$ and $\tau_O(K_c)$ denote $\tau_T(K_c; L)$ and $\tau_O(K_c; L)$, respectively, at the fixed system size L used for each crystal branch. Increasing K_c includes additional reciprocal vectors and raises the absolute values of τ_T and τ_O. Their ratio is much less cutoff sensitive and can be compared with the perfect-crystal result $\tau_O(K_c)/\tau_T(K_c) = 1$ from Eq. (27).

For the 2D hard-disk crystal, both metrics increase monotonically with ϕ at fixed K_c [Figs. 9(a)–9(d)]. To characterize

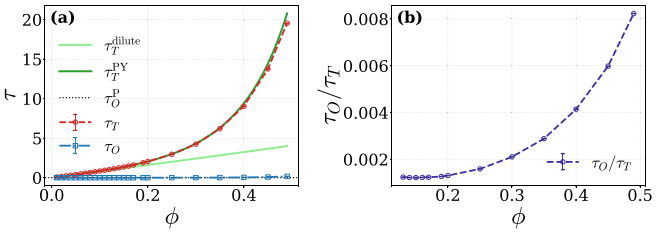


FIG. 8. Along the stable fluid branch of 3D equilibrium hard spheres, (a) τ_T and τ_O as functions of ϕ, together with the dilute-limit prediction $\tau_T^{\text{dilute}} = 8\phi$ and the Percus-Yevick prediction for τ_T, and (b) the ratio τ_O/τ_T. The ratio remains below 1% beyond the Poisson-reference regime, showing that bond-orientational order remains much smaller than translational order.

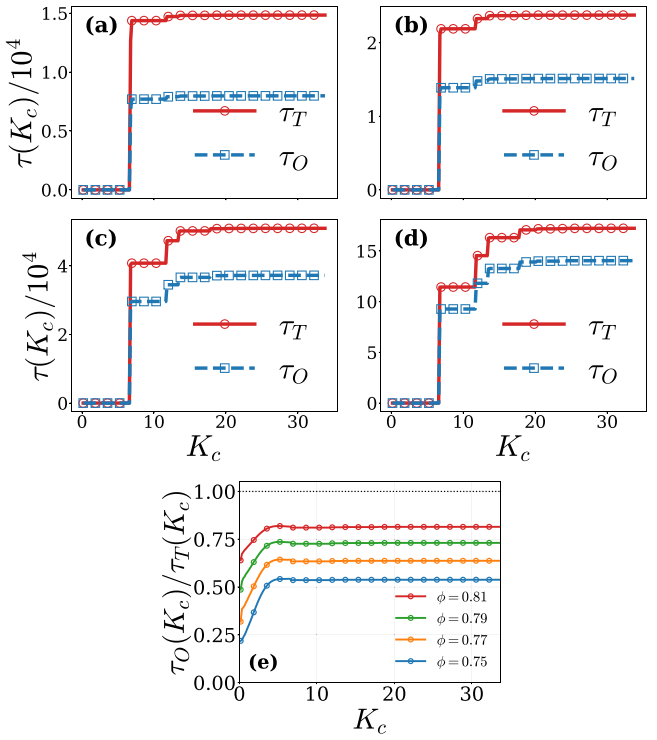


FIG. 9. The dependence of the order metrics on the cutoff wave number K_c for fixed system size L along the 2D hard-disk crystal branch. Panels (a)–(d) show $\tau_T/10^4$ and $\tau_O/10^4$ as functions of the reciprocal-space cutoff K_c for $\phi = 0.75$, 0.77, 0.79, and 0.81, respectively. The stepwise increases occur as successive Bragg shells enter the integration domain. Panel (e) shows τ_O/τ_T as a function of K_c for all four packing fractions. Although the absolute metrics receive substantial cutoff-dependent contributions from the Bragg peaks, over the higher-K_c range shown, their ratio approaches a stable, packing-fraction-dependent value that increases with ϕ.

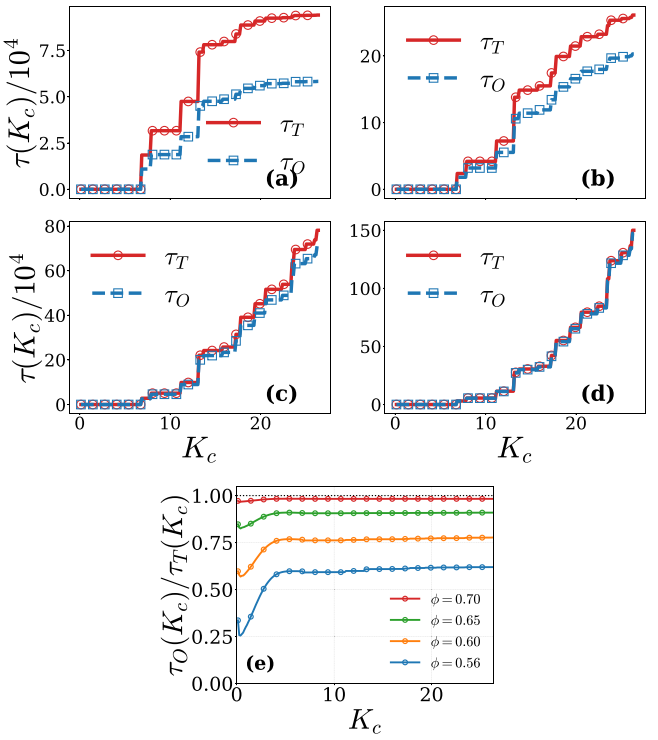


FIG. 10. The dependence of the order metrics on the cutoff wave number K_c for fixed system size L along the 3D hard-sphere fcc crystal branch using the 12 periodic nearest neighbors. Panels (a)–(d) show $\tau_T/10^4$ and $\tau_O/10^4$ as functions of the reciprocal-space cutoff K_c for $\phi = 0.56$, 0.60, 0.65, and 0.70, respectively. The stepwise increases occur as successive Bragg shells enter the integration domain. Panel (e) shows τ_O/τ_T as a function of K_c for all four packing fractions. Although the individual metrics receive substantial cutoff-dependent contributions from the Bragg peaks, over the higher-K_c range shown, their ratio approaches a stable, packing-fraction-dependent value that is nearly unity at the highest packing fraction.

the cutoff dependence at specified Bragg-shell cutoffs, we compare $K_c = 6.752$, corresponding to the first Bragg shell, with $K_c = 31.058$, the smallest sampled cutoff that fully includes the first ten Bragg shells. At $K_c = 6.752$, τ_O/τ_T increases from approximately 0.536 at $\phi = 0.75$ to 0.811 at $\phi = 0.81$; the corresponding values at $K_c = 31.058$ are 0.538 and 0.815 [Fig. 9(e)]. Thus, although the individual metrics receive substantial contributions as successive Bragg shells are included, the ratio changes by less than 0.7% upon increasing the cutoff from the first-shell value to a cutoff including the first ten Bragg shells for all four packing fractions. Translational and bond-orientational order are comparable throughout the sampled branch and become more nearly equal as ϕ increases.

For the 3D crystal branch, the primary calculation defines the orientational weights using the 12 periodic nearest neighbors, corresponding to the physical first coordination shell of the fcc lattice. With this definition, both metrics increase monotonically with ϕ at fixed K_c [Figs. 10(a)–10(d)]. To characterize the cutoff dependence at specified Bragg-shell cutoffs, we consider the smallest sampled cutoffs that fully include the first, fifth, tenth, and fifteenth Bragg shells, $K_c = 6.861$, 13.722, 20.582, and 25.992, respectively. At $\phi = 0.56$, τ_O/τ_T takes the corresponding values 0.591, 0.609, 0.617, and 0.619, whereas at $\phi = 0.70$ the ratio remains essentially unchanged at approximately 0.9825–0.9826 [Fig. 10(e)]. Thus, the cutoff dependence of the ratio is most pronounced at the lowest packing fraction, where it changes by approximately 4.8% from the first to the fifteenth Bragg shell. However, even at $\phi = 0.56$, the change from the tenth to the fifteenth shell is only approximately 0.3%, showing that the ratio becomes progressively less sensitive to the inclusion of higher Bragg shells. At $\phi = 0.70$, the corresponding first-to-fifteenth-shell change is only approximately 0.01%. A

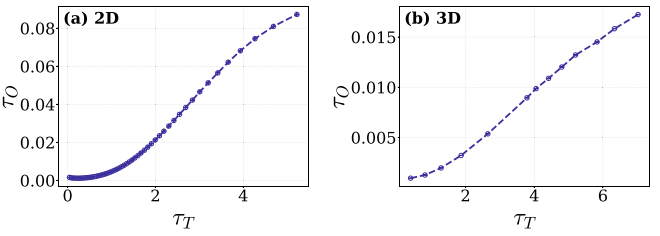


FIG. 11. Parametric relation between τ_O and τ_T along the RSA branches of (a) 2D hard disks and (b) 3D hard spheres.

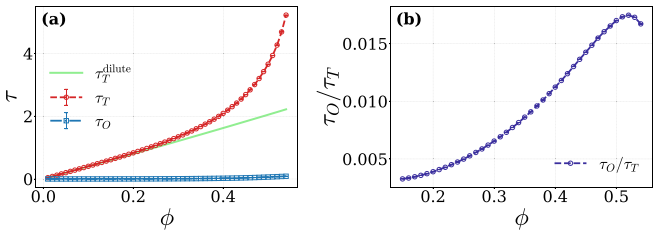


FIG. 12. Along the 2D RSA branch, (a) τ_T and τ_O as functions of ϕ, together with the dilute-limit prediction $\tau_T^{\rm dilute} = 4\phi$ for τ_T, and (b) the ratio τ_O/τ_T. Although τ_O remains subdominant, its magnitude relative to τ_T increases appreciably over most of the branch before decreasing slightly near saturation because of the more rapid growth of τ_T compared with τ_O.

diagnostic comparison using periodic Delaunay neighbors is presented in Appendix C. It leaves τ_T unchanged but reduces τ_O and τ_O/τ_T because the Delaunay construction includes neighbors beyond the first coordination shell.

Taken together, the equilibrium results reveal a clear fluid-crystal distinction. Bond-orientational order remains subdominant along both fluid branches, although its relative growth becomes pronounced near the upper end of the sampled 2D branch. By contrast, for the neighbor definitions used in the primary calculations, τ_T and τ_O are comparable along both crystal branches and approach equality as the perfect-crystal limit is approached. The 2D crystal values are based on one configuration at each packing fraction, whereas the 3D values are averages over ten configurations.

C. RSA packings

Figure 11 shows the parametric trajectories of the 2D and 3D RSA systems from the dilute regime to just below saturation. In both dimensions, τ_O increases monotonically with τ_T, but bond-orientational order remains a small fraction of translational order. Unless otherwise stated, the comparisons of the order metrics refer to sampled states beyond the Poisson-reference regime.

At low packing fractions, τ_T follows its dilute-limit prediction in both dimensions [Figs. 12(a) and 13(a)]. The Percus-Yevick curve in Fig. 13(a) is included only as an equilibrium hard-sphere reference in three dimensions. In two dimensions τ_O/τ_T increases from approximately 3.89×10^{-3}

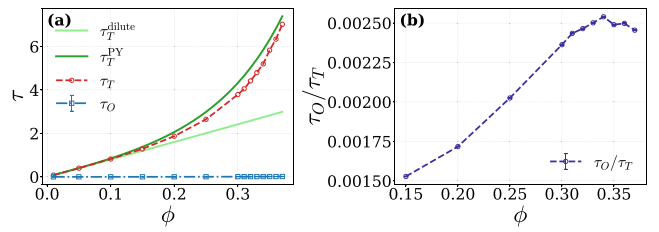


FIG. 13. Along the 3D RSA branch, (a) τ_T and τ_O as functions of ϕ, together with the dilute-limit prediction $\tau_T^{\rm dilute} = 8\phi$ and the Percus-Yevick prediction for τ_T, and (b) the ratio τ_O/τ_T. The ratio remains much smaller than unity throughout the branch and exhibits a slight downturn near saturation, as in two dimensions, reflecting the more rapid growth of τ_T compared with τ_O.

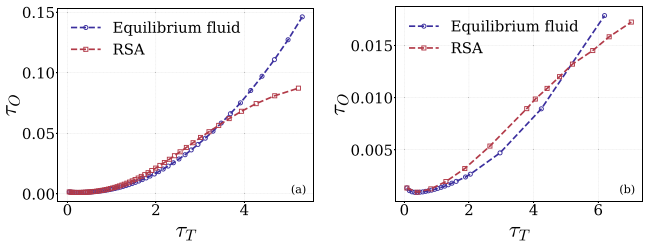


FIG. 14. Parametric comparison of τ_O and τ_T for equilibrium fluids and RSA packings in (a) two dimensions and (b) three dimensions. The two preparation protocols follow distinct trajectories in the (τ_T, τ_O) plane.

at $\phi = 0.20$ to 1.67×10^{-2} at $\phi = 0.54$, attaining a maximum of approximately 1.75×10^{-2} at $\phi = 0.52$ [Fig. 12(b)]. In three dimensions the variation is smaller: the ratio increases from approximately 1.72×10^{-3} at $\phi = 0.20$ to 2.45×10^{-3} at $\phi = 0.37$, with a maximum of approximately 2.54×10^{-3} at $\phi = 0.34$ [Fig. 13(b)]. Hence, τ_O remains below 2% of τ_T in two dimensions and below 0.3% in three. The ratio turns slightly downward close to saturation in both dimensions even though τ_O itself continues to increase. This downturn reflects the more rapid growth of τ_T compared with τ_O near saturation. It therefore represents a change in the relative growth rates of the two metrics, not a loss of bond-orientational order.

D. Comparison of equilibrium and RSA packings

Figure 14 compares the equilibrium-fluid and RSA trajectories in the (τ_T, τ_O) plane. In both dimensions, RSA packings have larger τ_O at moderate τ_T, whereas the equilibrium-fluid branch has larger τ_O at sufficiently high τ_T. Thus, comparable τ_T can correspond to different τ_O depending on the preparation protocol. This distinction is most pronounced in two dimensions, where the equilibrium-fluid trajectory bends upward at large τ_T because the relative growth of τ_O exceeds that of τ_T near the upper end of the sampled branch, whereas the RSA trajectory shows no analogous enhancement. In three dimensions τ_O remains much smaller than τ_T for both protocols, but their trajectories in the (τ_T, τ_O) plane remain distinct.

E. Stealthy hyperuniform ground states

We finally consider the disordered 2D SHU ground states specified in Sec. III C, using χ as the control parameter. Hyperuniformity is determined by the behavior of $S(k)$ as $k \to 0$, whereas τ_T integrates contributions over the full wave-number

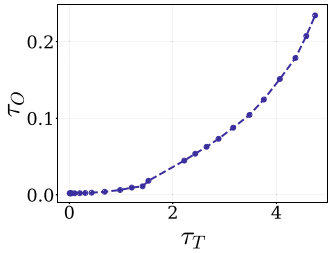


FIG. 15. Parametric relation between τ_O and τ_T within the 2D disordered SHU phase.

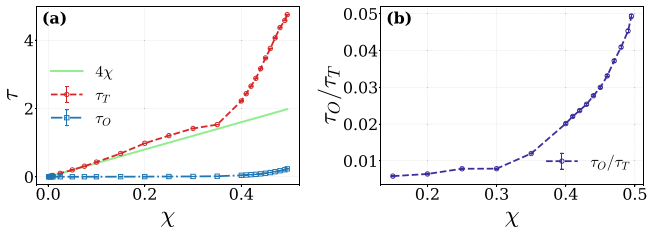


FIG. 16. Within the 2D disordered SHU phase, (a) τ_T and τ_O as functions of χ, together with the small-χ prediction $\tau_T \simeq 4\chi$, and (b) the ratio τ_O/τ_T. Although τ_O remains subdominant, its magnitude relative to τ_T increases as the ordering threshold at $\chi = 1/2$ is approached.

range [Eq. (10b)]. The two quantities therefore describe different aspects of the structure. Within the sampled disordered SHU phase, τ_O increases monotonically with τ_T (Fig. 15). The translational metric increases throughout the sampled range and follows the small-χ prediction $\tau_T \simeq 4\chi$ [Fig. 16(a)]. Although orientational order remains subdominant, τ_O/τ_T rises from approximately 6.42×10^{-3} at $\chi = 0.20$ to 4.93×10^{-2} at $\chi = 0.495$ [Fig. 16(b)]. Near the nominal disorder-to-order threshold at $\chi = 1/2$, $E_O > E_T$, and E_O/E_T increases overall from approximately 1.90 at $\chi = 0.41$ to 2.69 at $\chi = 0.48$ [Fig. 17]. Thus, τ_O/τ_T grows as the threshold is approached, even though τ_O remains much smaller than τ_T.

V. CONCLUSIONS AND DISCUSSION

The principal methodological advance of this work is that it places translational and bond-orientational order on a common two-point statistical footing. Whereas conventional metrics often quantify either positional order or spatially averaged local orientational order, the pair (τ_T, τ_O), defined in Eqs. (1) and (2), measures the integrated squared magnitude of the corresponding correlations and is therefore sensitive to both their amplitude and spatial persistence. Across nonhyperuniform equilibrium fluids, equilibrium crystals, nonhyperuniform RSA packings, and disordered SHU ground states, the pair (τ_T, τ_O) reveals structural distinctions associated with preparation protocol, dimensionality, and proximity to ordering.

Across the systems studied, τ_T and τ_O increase monotonically together along the sampled control-parameter paths (i.e., packing fraction ϕ in the case of the packing models and the stealthiness parameter χ in the case of disordered stealthy

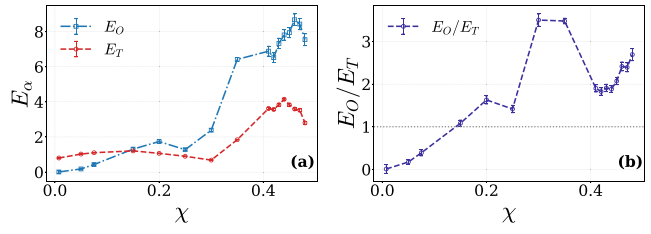


FIG. 17. Sensitivities E_T and E_O and their ratio E_O/E_T within the 2D disordered SHU phase. The responses vary across different ranges of χ, while near the ordering threshold the fractional growth of τ_O exceeds that of τ_T.

hyperuniform ground states), but their relative magnitudes vary substantially. Bond-orientational order remains subdominant along the equilibrium fluid branches of the hard-particle systems, the RSA branches, and within the disordered SHU phase, whereas τ_T and τ_O become comparable in magnitude along the sampled equilibrium crystal branches of the hard-particle systems. The sensitivities further show that τ_O grows more rapidly than τ_T in fractional terms near the upper end of the 2D equilibrium fluid branch and near the SHU ordering threshold.

It is useful to comment on the effect of dimensionality on the coupling between translational and orientational ordering in the case of the two hard-sphere models that we have considered. In equilibrium sphere packings, we have shown that orientational ordering relative to translational ordering is stronger along the fluid branch in two dimensions than in three. This weakening of the ratio also holds qualitatively as we go from 2D to 3D RSA packings. Moreover, the coupling between translational and orientational ordering is comparable along the crystal branches in two and three dimensions. We note that both translational and orientational ordering become weaker along the fluid branch of equilibrium hard spheres as well as RSA hard spheres as the space dimension increases beyond three because hard-sphere structures decorrelate with increasing d [43,48,49].

Several qualifications concerning the interpretation of these metrics should be noted. Because τ_T and τ_O are scalar integrated measures, it is clear that equal values do not imply identical underlying correlation functions or structures. The observed hierarchy $\tau_O < \tau_T$ is specific to the systems sampled here and should not be taken to be universal. In a hexatic phase, where bond-orientational correlations are quasi-long-ranged while translational correlations remain short-ranged [16,35], one may instead have $\tau_O > \tau_T$. The local orientational weights entering τ_O, $f_j = \psi_6(j)$ in two dimensions [Eq. (16)] and $\mathbf{f}_j = \{Q_{6m}(j)\}_{m=-6}^{6}$ in three [Eqs. (17) and (18)], depend on the definition of neighboring particles and bonds [50,51]. Comparisons of τ_O must therefore employ a consistent and physically appropriate neighbor-construction protocol. Determining how the relation between τ_O and τ_T depends on this choice, particularly for disordered systems, remains an interesting direction for future study. In the crystalline phases in both two and three dimensions, neither metric has a finite thermodynamic limit as $L \to \infty$. At fixed system size L, however, $\tau_T(K_c; L)$ and $\tau_O(K_c; L)$, defined in Eqs. (11) and (25), respectively, approach system-size-dependent values as $K_c \to \infty$. Over the range of cutoffs considered, the ratio τ_O/τ_T is substantially less cutoff sensitive than the individual metrics, and its stability has been checked directly as a function of K_c.

In future condensed-matter and statistical-physics studies, these metrics could be used to map structural pathways through freezing, melting, glass formation, jamming, self-assembly, and driven nonequilibrium transitions [8,21,52,53]. The joint (τ_T, τ_O) representation may help distinguish phases or metastable states with similar conventional pair structure, identify growing orientational organization before crystallization [54], and compare structures generated by different dynamics or processing histories [8]. Extensions to other rotational symmetries, multicomponent systems, anisotropic

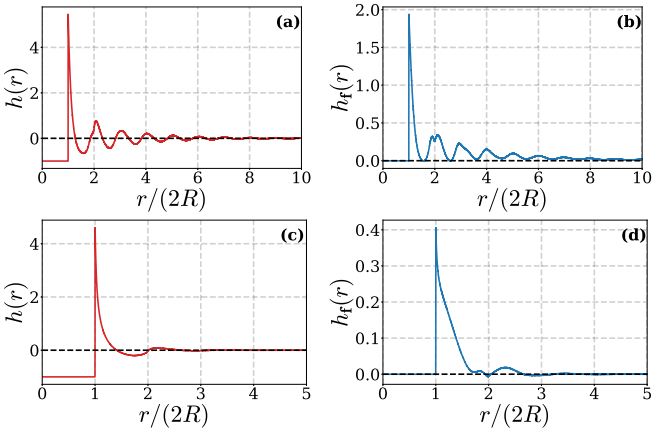


FIG. 18. Correlation functions for the 2D equilibrium hard-disk fluid at $\phi = 0.68$, the sampled fluid state closest to the liquid-hexatic transition (a), (b) and 2D RSA disk packings at $\phi = 0.54$, near saturation (c), (d). Panels (a) and (c) show $h(r)$, and panels (b) and (d) show $h_{\mathbf{f}}(r)$, defined in Eqs. (6) and (22), respectively. The orientational weight $f_j = \psi_6(j)$ is defined in Eq. (16). Separations are expressed as $r/(2R)$, where R is the disk radius. In both systems, the correlations decay well within the size of the simulation boxes.

particles, quasicrystals, active matter, and spin- or director-weighted configurations could provide symmetry-specific order coordinates [21,52,53]. A further direction is to construct analogous order metrics directly from explicit higher-order correlation functions, thereby quantifying structural information not fully captured by the present pair (τ_T, τ_O). The metric pair could also serve as collective variables in enhanced sampling [55], data-driven phase classification [56], and inverse-design optimization [41,42,52,57], especially if future work establishes how particular regions of the (τ_T, τ_O) plane relate to thermodynamic stability, kinetics, transport, mechanical response, or optical properties [42,58].

ACKNOWLEDGMENTS

We thank Samuel Dawley for numerical assistance with the independent verification of the equilibration of the crystal-branch configurations. We also thank Paul Steinhardt for valuable discussions. A.M. and S.T. were supported by the U.S. Army Research Office under Cooperative Agreement No. W911NF-22-2-0103, and we acknowledge the Princeton Institute for Computational Science and Engineering for the computational resources used in this work.

DATA AVAILABILITY

There are no publicly available research data or software supporting this paper. Requests for further information or data should be sent to the authors.

APPENDIX A: REPRESENTATIVE CORRELATION FUNCTIONS AND STRUCTURE FACTORS

In the following, we show representative correlation functions and structure factors for the model systems described in Sec. III. Figure 18 shows the correlations for the 2D equilibrium fluid and RSA systems, while Fig. 19 shows the structure factors for the 2D crystal. The 2D disordered SHU structure factors are shown in Fig. 20. Figure 21 shows the correlations for the 3D equilibrium fluid and RSA systems, and Fig. 22 shows the structure factors for the 3D crystal. For both crystal systems, the small-k behavior of $S(k)$ is consistent with the free-volume-theory prediction [10,47].

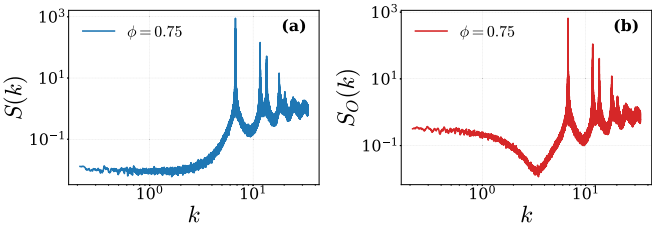


FIG. 19. Radially averaged structure factors for the 2D equilibrium hard-disk crystal at $\phi = 0.75$: (a) the translational structure factor $S(k)$ and (b) the bond-orientational structure factor $S_O(k)$. The orientational weight $f_j = \psi_6(j)$ is defined in Eq. (16).

APPENDIX B: ORIGIN AND VALIDATION OF THE POISSON REFERENCE VALUE

For a homogeneous Poisson point process, $g_2(r) = 1$ and hence $h(r) = 0$, so that $\tau_T = 0$. The orientational marks used to construct τ_O, however, are not independent marks assigned independently of the particle positions. They are determined from the local periodic Delaunay geometry. Nearby particles can therefore have correlated marks because their local neighbor environments overlap and may contain common bonds or common neighbors. Thus, although the particle centers form a Poisson point process and the mean orientational mark vanishes by isotropy, the weighted total correlation function $h_{\mathbf{f}}(r)$ need not vanish at short distances. The resulting nonzero τ_O^{P} [Eq. (24a)] is therefore a reference value induced by the geometrical construction of the marks, rather than evidence of macroscopic bond-orientational order.

To separate this geometry-induced contribution from the finite-sampling background, we randomly shuffle the

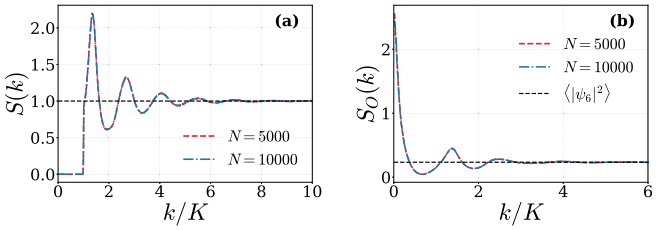


FIG. 20. Representative radially averaged structure factors for the 2D disordered SHU ground-state ensemble at $\chi = 0.495$, the sampled state closest to the ordering threshold at $\chi = 1/2$: (a) the unweighted structure factor $S(k)$ and (b) the bond-orientational structure factor $S_O(k)$. The wave number is reported as the dimensionless quantity k/K, where K is the width of the stealthy exclusion region. Both structure factors are essentially unchanged upon increasing the system size from $N = 5000$ to $N = 10\,000$. The horizontal black dashed lines indicate unity in panel (a) and the self-contribution $\langle|\psi_6|^2\rangle$ in panel (b).

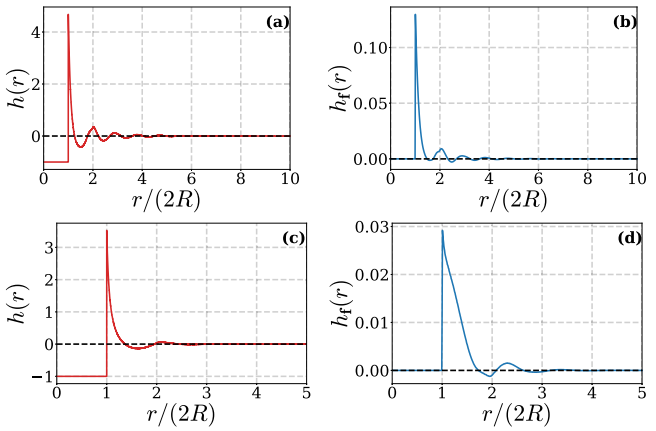


FIG. 21. Correlation functions for the 3D equilibrium hard-sphere fluid at $\phi = 0.49$, the sampled fluid state closest to freezing (a), (b) and 3D RSA sphere packings at $\phi = 0.37$, near saturation (c), (d). Panels (a) and (c) show $h(r)$, and panels (b) and (d) show $h_{\mathbf{f}}(r)$, defined in Eqs. (6) and (22), respectively. The orientational weight $\mathbf{f}_j = \{Q_{6m}(j)\}_{m=-6}^{6}$ is constructed using periodic Delaunay neighbors and defined in Eq. (17). Separations are expressed as $r/(2R)$, where R is the sphere radius. In both systems, the correlations decay well within the size of the simulation boxes.

calculated orientational marks among the same particle positions. This procedure leaves the point configuration and the one-particle distribution of the marks unchanged, but removes the association between each mark and the local geometry from which it was calculated. Consequently, any persistent difference between the original and shuffled results isolates the contribution arising from correlations among the geometry-derived marks.

Figure 23 shows the system-size dependence of the original and shuffled values in two and three dimensions. In both cases, the original Poisson value approaches a finite constant as the number of particles increases, whereas the shuffled value decreases toward zero approximately as a power law in N. This behavior confirms that the nonzero Poisson reference value of τ_O survives in the thermodynamic limit and originates from short-range correlations among the Delaunay-derived orientational marks, while the shuffled contribution is a finite-sampling effect.

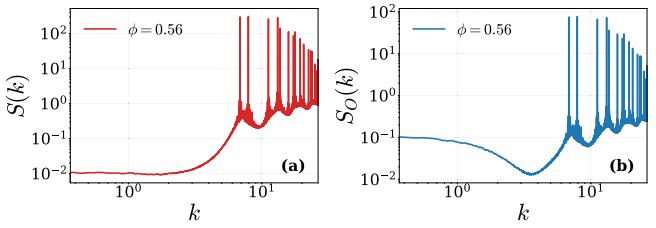


FIG. 22. Radially averaged structure factors for the 3D equilibrium hard-sphere fcc crystal at $\phi = 0.56$: (a) the translational structure factor $S(k)$ and (b) the bond-orientational structure factor $S_O(k)$. The orientational weight $\mathbf{f}_j = \{Q_{6m}(j)\}_{m=-6}^{6}$ is constructed using 12 periodic nearest neighbors and defined in Eq. (17).

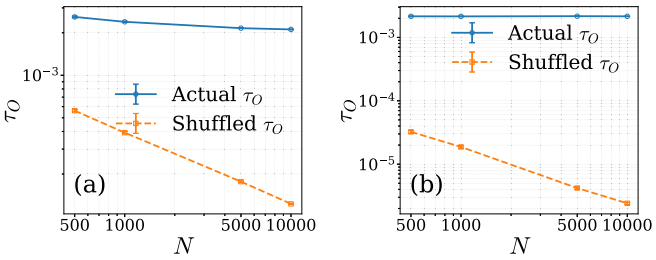


FIG. 23. System-size dependence of τ_O for Poisson point configurations in (a) two dimensions and (b) three dimensions, using the original Delaunay-derived orientational marks and the same marks randomly shuffled among the particle positions. The original values approach finite constants, whereas the shuffled values decrease toward zero approximately as power laws in N.

APPENDIX C: COMPARISON OF τ METRICS FOR THE 3D EQUILIBRIUM CRYSTAL BRANCH USING PERIODIC DELAUNAY NEIGHBORS

Periodic Delaunay neighbors provide a diagnostic test of the neighbor definition. As in the primary crystal calculation, $\tau_T(K_c)$ and $\tau_O(K_c)$ are evaluated at fixed system size L using the same common radial cutoff K_c. Because τ_T depends only on particle positions, it is unchanged, whereas τ_O depends on the bonds used to construct the local Q_6 weights. The Delaunay construction includes neighbors beyond the 12-neighbor first coordination shell, reducing the local Q_6 amplitudes and suppressing τ_O. At $\phi = 0.70$, the ratio approaches

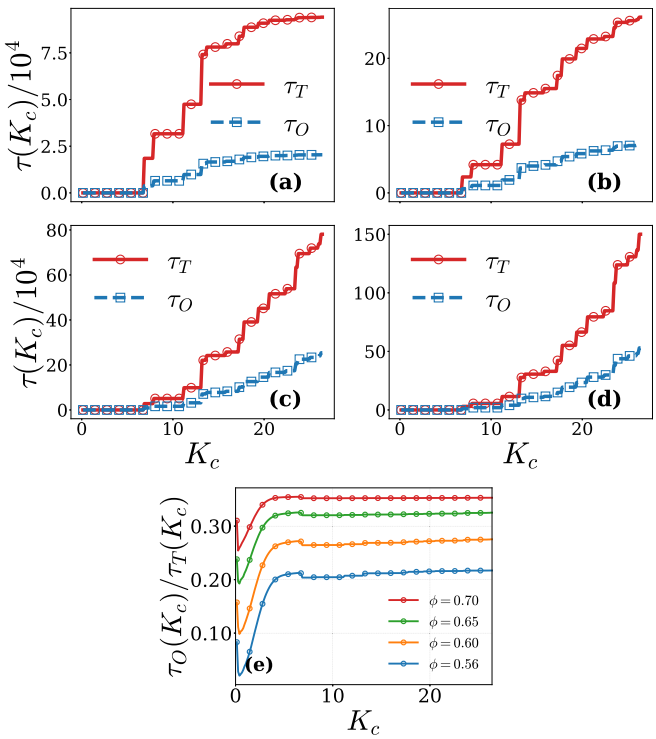


FIG. 24. Corresponding results for the 3D fcc crystal branch using periodic Delaunay neighbors as a diagnostic comparison at fixed system size L. The additional neighbors included by the Delaunay construction suppress τ_O and consequently reduce τ_O/τ_T, while leaving τ_T unchanged.

approximately 0.35 over the higher-K_c range shown [Fig. 24]. We therefore use the 12-neighbor definition, which isolates the first coordination shell of the fcc lattice, for the primary results presented in Sec. IV B 3 and retain the Delaunay calculation solely as a diagnostic of the sensitivity of τ_O to the neighbor definition.

[1] J.-P. Hansen and I. R. McDonald, *Theory of Simple Liquids: With Applications to Soft Matter* (Academic Press, Cambridge, MA, 2013).

[2] S. Torquato, *Random Heterogeneous Materials: Microstructure and Macroscopic Properties*, Interdisciplinary Applied Mathematics Vol. 16 (Springer, New York, 2002).

[3] P. M. Chaikin and T. C. Lubensky, *Principles of Condensed Matter Physics* (Cambridge University Press, Cambridge, 1995).

[4] D. Frenkel and B. Smit, *Understanding Molecular Simulation* (Elsevier, New York, 2023).

[5] P. J. Steinhardt and S. Ostlund, *The Physics of Quasicrystals* (World Scientific, Singapore, 1987).

[6] D. Levine and P. J. Steinhardt, Quasicrystals: A new class of ordered structures, Phys. Rev. Lett. **53**, 2477 (1984).

[7] S. Torquato, T. M. Truskett, and P. G. Debenedetti, Is random close packing of spheres well defined?, Phys. Rev. Lett. **84**, 2064 (2000).

[8] T. M. Truskett, S. Torquato, and P. G. Debenedetti, Towards a quantification of disorder in materials: Distinguishing equilibrium and glassy sphere packings, Phys. Rev. E **62**, 993 (2000).

[9] A. R. Kansal, T. M. Truskett, and S. Torquato, Nonequilibrium hard-disk packings with controlled orientational order, J. Chem. Phys. **113**, 4844 (2000).

[10] S. Torquato, Physics of sphere packings, Nat. Rev. Phys. **8**, 261 (2026).

[11] R. E. Nettleton and M. S. Green, Expression in terms of molecular distribution functions for the entropy density in an infinite system, J. Chem. Phys. **29**, 1365 (1958).

[12] J. R. Errington and P. G. Debenedetti, Relationship between structural order and the anomalies of liquid water, Nature (London) **409**, 318 (2001).

[13] J. R. Errington, P. G. Debenedetti, and S. Torquato, Cooperative origin of low-density domains in liquid water, Phys. Rev. Lett. **89**, 215503 (2002).

[14] J. R. Errington, P. G. Debenedetti, and S. Torquato, Quantification of order in the Lennard-Jones system, J. Chem. Phys. **118**, 2256 (2003).

[15] B. I. Halperin and D. R. Nelson, Theory of two-dimensional melting, Phys. Rev. Lett. **41**, 121 (1978).

[16] D. R. Nelson and B. I. Halperin, Dislocation-mediated melting in two dimensions, Phys. Rev. B **19**, 2457 (1979).

[17] P. Keim, G. Maret, and H. H. von Grünberg, Frank's constant in the hexatic phase, Phys. Rev. E **75**, 031402 (2007).

[18] C. H. Mak, Large-scale simulations of the two-dimensional melting of hard disks, Phys. Rev. E **73**, 065104(R) (2006).

[19] A. L. Thorneywork, J. L. Abbott, D. G. A. L. Aarts, and R. P. A. Dullens, Two-dimensional melting of colloidal hard spheres, Phys. Rev. Lett. **118**, 158001 (2017).

[20] Y. Han, N. Y. Ha, A. M. Alsayed, and A. G. Yodh, Melting of two-dimensional tunable-diameter colloidal crystals, Phys. Rev. E **77**, 041406 (2008).

[21] P. J. Steinhardt, D. R. Nelson, and M. Ronchetti, Bond-orientational order in liquids and glasses, Phys. Rev. B **28**, 784 (1983).

[22] P. Rein ten Wolde, M. J. Ruiz-Montero, and D. Frenkel, Numerical calculation of the rate of crystal nucleation in a Lennard-Jones system at moderate undercooling, J. Chem. Phys. **104**, 9932 (1996).

[23] U. Gasser, E. R. Weeks, A. Schofield, P. N. Pusey, and D. A. Weitz, Real-space imaging of nucleation and growth in colloidal crystallization, Science **292**, 258 (2001).

[24] W. Lechner and C. Dellago, Accurate determination of crystal structures based on averaged local bond order parameters, J. Chem. Phys. **129**, 114707 (2008).

[25] T. Kawasaki and H. Tanaka, Formation of a crystal nucleus from liquid, Proc. Natl. Acad. Sci. USA **107**, 14036 (2010).

[26] M. Leocmach and H. Tanaka, Roles of icosahedral and crystal-like order in the hard spheres glass transition, Nat. Commun. **3**, 974 (2012).

[27] M. D. Rintoul and S. Torquato, Metastability and crystallization in hard-sphere systems, Phys. Rev. Lett. **77**, 4198 (1996).

[28] S. Torquato, G. Zhang, and F. H. Stillinger, Ensemble theory for stealthy hyperuniform disordered ground states, Phys. Rev. X **5**, 021020 (2015).

[29] E. Lomba, J.-J. Weis, and S. Torquato, Disordered hyperuniformity in two-component nonadditive hard-disk plasmas, Phys. Rev. E **96**, 062126 (2017).

[30] In Ref. [29], it is shown that the excess entropy [8] is clearly related to the τ_T order metric. The advantage of τ_T over excess entropy is that the former has both direct- and Fourier-space representations, which enable accurate capture of both short- and long-wavelength translational correlations.

[31] G. Zhang, F. H. Stillinger, and S. Torquato, The perfect glass paradigm: Disordered hyperuniform glasses down to absolute zero, Sci. Rep. **6**, 36963 (2016).

[32] M. A. Klatt, J. Lovrić, D. Chen, S. C. Kapfer, F. M. Schaller, P. W. A. Schönhöfer, B. S. Gardiner, A.-S. Smith, G. E. Schröder-Turk, and S. Torquato, Universal hidden order in amorphous cellular geometries, Nat. Commun. **10**, 811 (2019).

[33] S. Torquato, G. Zhang, and M. De Courcy-Ireland, Hidden multiscale order in the primes, J. Phys. A: Math. Theor. **52**, 135002 (2019).

[34] M. A. Klatt, J. Kim, and S. Torquato, Cloaking the underlying long-range order of randomly perturbed lattices, Phys. Rev. E **101**, 032118 (2020).

[35] S. Torquato, J. Kim, M. A. Klatt, R. Car, and P. J. Steinhardt, Hyperuniformity of weighted particle systems, Phys. Rev. X **16**, 011042 (2026).

[36] S. Torquato and F. H. Stillinger, Local density fluctuations, hyperuniformity, and order metrics, Phys. Rev. E **68**, 041113 (2003).

[37] G. Zhang and S. Torquato, Precise algorithm to generate random sequential addition of hard hyperspheres at saturation, Phys. Rev. E **88**, 053312 (2013).

[38] R. D. Batten, F. H. Stillinger, and S. Torquato, Classical disordered ground states: Super-ideal gases and stealth and equi-luminous materials, J. Appl. Phys. **104**, 033504 (2008).

[39] E. P. Bernard and W. Krauth, Two-step melting in two dimensions: First-order liquid-hexatic transition, Phys. Rev. Lett. **107**, 155704 (2011).

[40] S. Torquato, J. Kim, and M. A. Klatt, Local number fluctuations in hyperuniform and nonhyperuniform systems: Higher-order moments and distribution functions, Phys. Rev. X **11**, 021028 (2021).

[41] S. Torquato, M. Skolnick, and J. Kim, Local order metrics for two-phase media across length scales, J. Phys. A: Math. Theor. **55**, 274003 (2022).

[42] W. Shi, Y. Jiao, and S. Torquato, Three-dimensional construction of hyperuniform, nonhyperuniform, and antihyperuniform disordered heterogeneous materials and their transport properties via spectral density functions, Phys. Rev. E **111**, 035310 (2025).

[43] M. Skoge, A. Donev, F. H. Stillinger, and S. Torquato, Packing hyperspheres in high-dimensional Euclidean spaces, Phys. Rev. E **74**, 041127 (2006).

[44] N. Metropolis, A. W. Rosenbluth, M. N. Rosenbluth, A. H. Teller, and E. Teller, Equation of state calculations by fast computing machines, J. Chem. Phys. **21**, 1087 (1953).

[45] O. U. Uche, S. Torquato, and F. H. Stillinger, Collective coordinate control of density distributions, Phys. Rev. E **74**, 031104 (2006).

[46] B. Efron and R. J. Tibshirani, *An Introduction to the Bootstrap*, Monographs on Statistics and Applied Probability Vol. 57 (Chapman & Hall, New York, 1993).

[47] H. Wang, D. A. Huse, and S. Torquato, Hole statistics of equilibrium 2D and 3D hard-sphere crystals, J. Chem. Phys. **161**, 074106 (2024).

[48] S. Torquato and F. H. Stillinger, New conjectural lower bounds on the optimal density of sphere packings, Exp. Math. **15**, 307 (2006).

[49] S. Torquato, Effect of dimensionality on the continuum percolation of overlapping hyperspheres and hypercubes, J. Chem. Phys. **136**, 054106 (2012).

[50] J. A. van Meel, L. Filion, C. Valeriani, and D. Frenkel, A parameter-free, solid-angle based, nearest-neighbor algorithm, J. Chem. Phys. **136**, 234107 (2012).

[51] W. Mickel, S. C. Kapfer, G. E. Schröder-Turk, and K. Mecke, Shortcomings of the bond orientational order parameters for the analysis of disordered particulate matter, J. Chem. Phys. **138**, 044501 (2013).

[52] S. Torquato, Inverse optimization techniques for targeted self-assembly, Soft Matter **5**, 1157 (2009).

[53] P. Digregorio, D. Levis, A. Suma, L. F. Cugliandolo, G. Gonnella, and I. Pagonabarraga, Full phase diagram of active Brownian disks: From melting to motility-induced phase separation, Phys. Rev. Lett. **121**, 098003 (2018).

[54] J. Russo and H. Tanaka, The microscopic pathway to crystallization in supercooled liquids, Sci. Rep. **2**, 505 (2012).

[55] S. Auer and D. Frenkel, Prediction of absolute crystal-nucleation rate in hard-sphere colloids, Nature (London) **409**, 1020 (2001).

[56] J. Carrasquilla and R. G. Melko, Machine learning phases of matter, Nat. Phys. **13**, 431 (2017).

[57] C. E. Maher and S. Torquato, Local order metrics for many-particle systems across length scales, Phys. Rev. Res. **6**, 033262 (2024).

[58] J. Kim and S. Torquato, Extraordinary optical and transport properties of disordered stealthy hyperuniform two-phase media, J. Phys.: Condens. Matter **36**, 225701 (2024).